Ore Geology Reviews 73 (2016) 540–554

Contents lists available at ScienceDirect

Ore Geology Reviews

journal homepage: www.elsevier.com/locate/oregeorev

Proximal and remote spectroscopic characterisation of regolith in the Albany–Fraser Orogen (Western Australia)

C. Laukamp *, W. Salama, I. González-Álvarez

CSIRO Mineral Resources Flagship, 26 Dick Perry Avenue, Kensington, WA 6151, Australia

ARTICLE INFO

Article history:
Received 28 April 2015
Received in revised form 30 September 2015
Accepted 2 October 2015
Available online 9 October 2015

Keywords:
ASTER
HyLogging
Regolith
Remote sensing
Albany–Fraser Orogen
Mineral exploration

ABSTRACT

Vast parts of the Australian continent are prospective for precious and base metal mineralisation, but exploration is hindered by extensive cover of often deeply reaching regolith. New operational exploration methods are required that can help to characterise the cover and provide information about bedrock signatures. This paper shows how mineral mapping information from a combination of satellite multispectral Advanced Spaceborne Thermal Emission and Reflection Radiometer (ASTER) imagery and drill core hyperspectral profiling data (HyLogging™) can be used to unravel the regolith stratigraphy and to describe regional variations of regolith landforms, delivering important information for mineral exploration.

The case study is located in the Neale tenements in the northeastern Albany–Fraser Orogen (Western Australia), which is prospective for Tropicana-style gold mineralisation. By interpretation of indicator minerals from hyperspectral drill hole logging data the regolith stratigraphy atop a metamorphic basement, comprising saprock, ferrugineous saprolite, kaolinitic saprolite, silcrete and transported cover, is recorded in cm-detail. Important mineralogical parameters extracted from the hyperspectral subsurface data and validated by XRD and FTIR, are 1) the abundance and type of iron oxides, 2) the abundance and crystallinity of kaolinite, 3) the abundance and composition of primary minerals, such as white mica, and 4) the abundance of quartz.

The HyLogging™ data served as ground control points for mineral mapping information provided by CSIRO's ASTER Geoscience Products, which are a collection of mineral maps that highlight variations in the abundance, type or chemistry of selected mineral groups. Key ASTER Geoscience Products for regolith characterisation were the Ferric Oxide and AlOH abundance and composition images. The comparison of the surface with the subsurface data suggests three major different regolith landforms, including erosional, depositional and relict areas, which were used to generate a map showing transported versus relict and erosional areas. Erosional domains were mapped out in great detail, providing important information for exploration in saprolite dominated areas. Furthermore, source areas of transported material could be identified, which may help to understand the distribution of geochemical signatures collected during, for example, geochemical soil sampling projects.

1. Introduction

An emerging generation of optical sensing technologies, operating from drill core to space based platforms, provides the opportunity for explorers to use the derived mineral information for more efficient mineral deposit discovery, including in areas obscured by regolith cover. Operational technologies to date include the satellite multispectral imaging sensor ASTER (Advanced Spaceborne Thermal Emission and Reflection Radiometer; Yamaguchi et al., 1999) and the hyperspectral drill core logging system HyLogging™ (Huntington et al., 2005), providing detailed information to explorers about the abundance and composition of minerals. The multispectral ASTER data can help to characterise regolith environments and mineral systems from the continent to the prospect scale down to 15 m/pixel spatial resolution (Rowan et al., 2003; Hewson et al., 2005; Hewson and Cudahy, 2010; Laukamp, 2013). Examples of successful application of ASTER data for mineral exploration range from targeting iron ore in banded iron formations (Duuring et al., 2012) to delineation of hydrothermal alteration associated with gold mineralisation (Witt et al., 2013). The HyLogging™ system provides spatially dense (down to 1 cm) drill hole information about the abundance, composition and/or crystallinity of visible and infrared active mineral species (Haest et al., 2012a). This detailed mineralogical information can be applied for the characterisation of regolith and bedrock lithologies, such as the separation of saprolite and transported material, depth to bedrock or hydrothermal alteration patterns (Cudahy et al., 2009; Haest et al., 2012a, 2012b; Tappert et al., 2013). The characterisation of regolith landforms is paramount for explorers in regions such as the Albany–Fraser Orogen.

Regolith landforms in the northeastern Albany–Fraser Orogen are similar to those of the Yilgarn Craton (González-Álvarez et al. (in this issue-a)), where they can be separated according to Anand and Paine

* Corresponding author.
E-mail address: Carsten.Laukamp@csiro.au (C. Laukamp).

http://dx.doi.org/10.1016/j.oregeorev.2015.10.003
0169-1368/

(2002) into three major regolith landform units for the Yilgarn Craton: 1) Sands, ferruginous gravels and duricrust-dominated terrains (relict), 2) Saprolite and bedrock-dominated terrains (erosional) and 3) Sediment-dominated terrains (depositional). These three regolith landforms are not only characterised by a distinct morphology, but also by a distinct mineralogy. In regolith systems, clay minerals and iron oxides develop in certain levels of the regolith stratigraphy, depending on the source/bed rocks and the physicochemical conditions of the environment (e.g. ground water chemistry). Kaolinite and halloysite for example are typical weathering products of feldspars (±muscovite) and are more abundant in regolith materials sourced from mafic and felsic rocks than from ultramafic rocks (Anand and Paine, 2002). This is in contrast to smectites, which form especially at the base of deeply weathered profiles in dry or poorly drained conditions (Anand and Paine, 2002). Smectites are weathering products of "primary" minerals, with high Fe/Al smectites forming from mafic rocks. In upper levels of the regolith smectite weathers to kaolinite and goethite.

Regolith cover in the Albany–Fraser Orogen is extensive and outcrops of bedrocks are scarce. Locally, only breakaways provide ready insights into bedrock lithologies, though the respective material is usually heavily weathered. An advanced mineralogical characterisation and understanding of the regolith materials and landforms (including weathered bedrock) is crucial in order to 1) help distinguishing transported from residual material (important for mineral exploration), and 2) characterise mineral assemblages at a district to regional scale distribution that reflect the type of concealed bedrock and/or alteration systems. These can provide insights into the mechanisms behind the lateral and vertical distribution of indicator minerals in weathering profiles.

The present study is focused mainly on the characterisation of regolith landforms and associated mineralogical variations in a selected area in the northeastern Albany–Fraser Orogen using reflectance spectroscopic techniques, validated by FTIR, XRD and geochemistry. For this, mineral group maps, derived from multispectral remote sensing data (i.e. ASTER), and hyperspectral subsurface data (i.e. HyLogging™) were acquired from the south part of the Neale tenement (held by Beadell Resources Ltd.) located about 385 km southeast of Kalgoorlie and 60 km northeast from the Tropicana gold deposit, in the Eastern Biranup Zone of the northeastern Albany–Fraser Orogen (Fig. 1). This study evaluates 1) whether the detailed mineralogy obtained from the HyLogging™ data can be extrapolated to mineralogical expressions at the surface using the ASTER data, and 2) if the remote sensing data can be used to generate regolith maps, that may assist mineral exploration in regolith-dominated terrains (RDT; Anand, in this issue; Butt, 2016–in this issue; González-Álvarez et al. (in this issue-b)). For validation of the reflectance spectroscopic data, HyLogging™ results were compared with XRD and FTIR analyses, providing a detailed understanding of the mineral assemblages in the regolith profile.

2. Geological setting

The study area is located in the Eastern Biranup Zone (Kirkland et al., 2011) of the northeastern Albany–Fraser Orogen. The Eastern Biranup Zone comprises intensely deformed orthogneiss, metagabbro and paragneiss (Spaggiari et al., 2011). Kirkland et al. (2011) described the Albany–Fraser Orogen as a Mesoproterozoic continent–continent collision zone between the Archaean Yilgarn Craton to the northwest and the Gawler Craton to the east. The area in contact with the Gawler Craton is covered by Cenozoic sediments of the Eucla Basin.

In the study area (Fig. 1), the Palaeoproterozoic Bobbie Point Metasyenogranite is thrusted northwest upon the Palaeozoic Paterson Formation along the northeast trending Cundeelee fault (Spaggiari et al., 2011, 2014a). Northeast trending shear zones separate the Bobbie Point Metasyenogranite from the Atlantis prospect located in the McKay Creek Metasyenogranite, and metagranites of the Biranup zone further southeast (Fig. 1). The McKay Creek Metasyenogranite (Fig. 1), hosting the Hercules and Atlantis prospects, can be mingled with metagrabbro and may include intrusions of the Bobbie Point Metasyenogranite and remnants of Archaean rocks (Spaggiari et al., 2014b and references therein). Doyle et al. (2015) described subeconomic gold mineralisation in the Voodoo Child domain further to the southwest.

Gold mineralisation is associated with "silica sericite alteration" along the Hercules Shear Zone and along a major granite gneiss/paragneiss contact (Spaggiari et al., 2014b). The Hercules trend is prospective for Tropicana-style mineralisation and is characterised by a metachert intersected close to the contact between a garnet gneiss in the east and a granite gneiss in the west. According to Beadell Resources Ltd., about 30 to 40 m of transported regolith can cover the mineralised

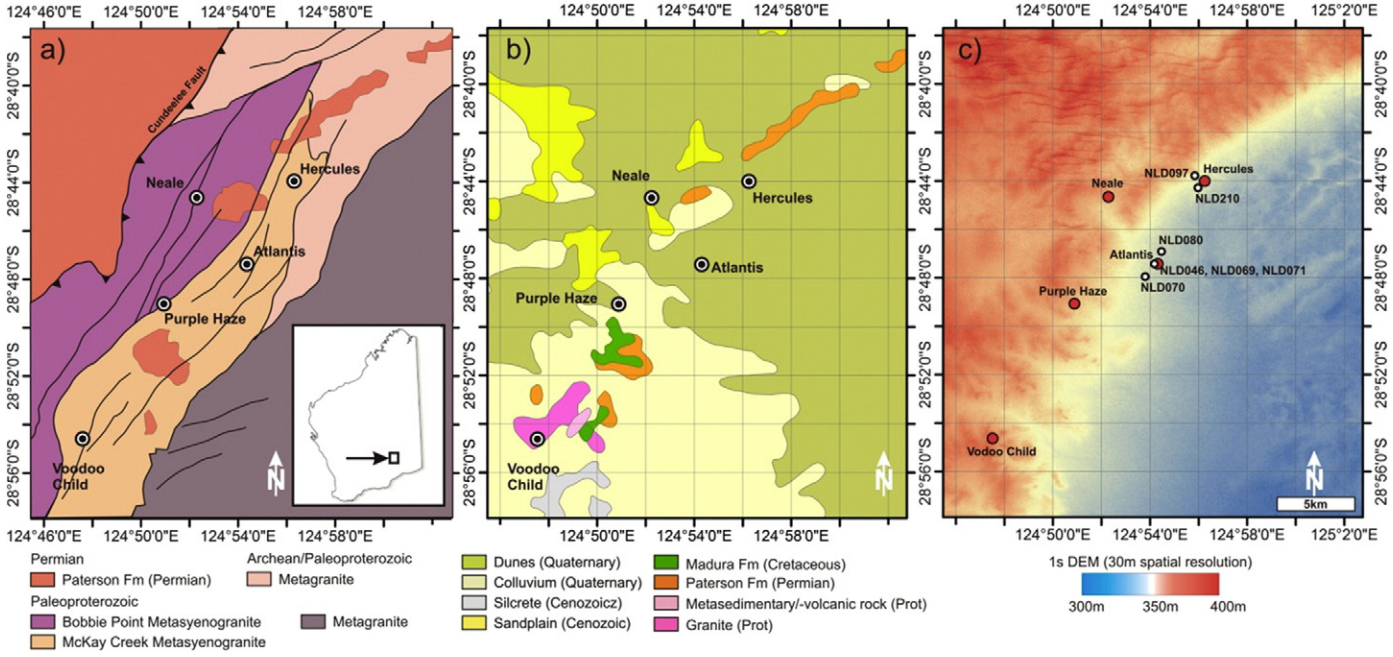

Fig. 1. a) Basement geology of the case study area (modified after Spaggiari and Pawley (2012); b) Surface geological map (1 M, Stewart et al., 2008); c) DEM (Gallant et al., 2011) showing location of drill cores (NLD046 to NLD210) from the Hercules and Atlantis sites, scanned with the HyLogging™ system. Neale, Purple Haze and Voodoo Child are further exploration sites.

basement rocks or the basement rocks are generally stripped of any significant saprolite (e.g. around Vodoo Child, Fig. 1).

2.1. Regolith landforms, mineralogy and geochemistry

The Albany–Fraser Orogen is covered to about 85% of regolith, which can reach up to 150 m thickness. Weathering profiles are a consequence of a paleoclimatic evolution from humid and sub-tropical to arid and semi-arid weathering and the related climatic overprinting, which masks geochemical footprints of buried mineral systems. Addressing these issues, González-Álvarez et al. (in this issue-a) classified four regolith settings in the Albany–Fraser Orogen, namely 1) Albany setting featuring shallow weathered profiles with minimal regolith thickness (i.e. 0 to 15 m), 2) Kalgoorlie–Norseman setting with an intense and variably deep weathering profile of at least 20 m and relict landscapes with erosional breaks, 3) Esperance setting, characterised by sand dunes with thin exposure of surface regolith stratigraphy, and 4) silcrete and transported material covering a deep in situ weathering profile as the Neale setting (Salama et al., 2016–in this issue). According to Tille (2006) the northeastern part of the Albany–Fraser Orogen is characterised by sandplains, dunes and minor gravelly and calcrete plains, which are typical for the Southern Great Victoria Desert Zone. These recent sediments were deposited on sedimentary rocks of the Gunbarrel (e.g. conglomerates of the Paterson Formation) and Officer Basin. Salama et al. (2016–in this issue) described an undulating basement morphology, which was filled in and covered by transported sands and gravels. The regolith–bedrock interface is located at about 70 m depth, generally increasing to the SE and/or NE. Shear zones possibly played a significant role in the palaeotopographic variations, by controlling the orientation of palaeodrainage systems.

Salama et al. (2016–in this issue) provide a detailed stratigraphic, mineralogical and geochemical characterisation of regolith in the Neale tenement. The regolith stratigraphy consists of a transported blanket of ferruginous sands, gravels and lateritic pisoliths and nodules, cemented at depth by Fe-stained kaolinite, which overly in situ deeply weathered granitoids, gneisses and mafic rocks. Based on petrographical and geochemical analyses, four units in the in situ regolith profile can be described, namely 1) saprock, 2) lower ferruginous saprolite, 3) upper kaolinitic saprolite and 4) silcrete. The four in situ regolith units and the blanket of transported cover are recognisable in a profile generated from rock chip data (Fig. 2). Geochemical analyses (Salama et al., 2016–in this issue) revealed an enrichment of SiO_2, MgO, Na_2O, K_2O, Ba and Rb in granitic bedrocks whereas the same elements are depleted in mafic bed rocks, which are also characterised by enrichment in all transition metals. The lower ferruginous saprolite traces a combination of the geochemical signatures of the granitic and mafic bedrocks (i.e. enrichment in alkali, alkaline earth and transition metals), suggesting heterogeneities in the bedrock composition. This geochemical signature is replaced in the upper kaolinitic saprolite by depletion in alkali and alkaline earth elements as well as selected transition metals, including Ni, Co, Cr, Zn and Cu, and enrichment of SiO_2, Al_2O_3, Th, Zr, Ba, Sr and Pb. The lower ferruginous saprolite is dominated by quartz, feldspar, kaolinite, as well as goethite after ferromagnesian minerals (i.e. biotite, hornblende, garnet, pyroxene, chlorite), titanite after ilmenite and jarosite after pyrite. In contrast, the upper kaolinitic saprolite contains mainly quartz floating in kaolinite ± illite. The silcrete duricrust is mainly enriched in SiO_2 and TiO_2, forming discontinuous lenses of quartz, anatase and zircon cement that laterally change into poorly cemented kaolinitic grits, therefore only locally protecting the underlying weathering profile.

3. Mineral reflectance spectroscopy

The crystallinity of kaolinite group minerals, which can be inferred from hyperspectral data (Crowley and Vergo, 1988), can be used as a

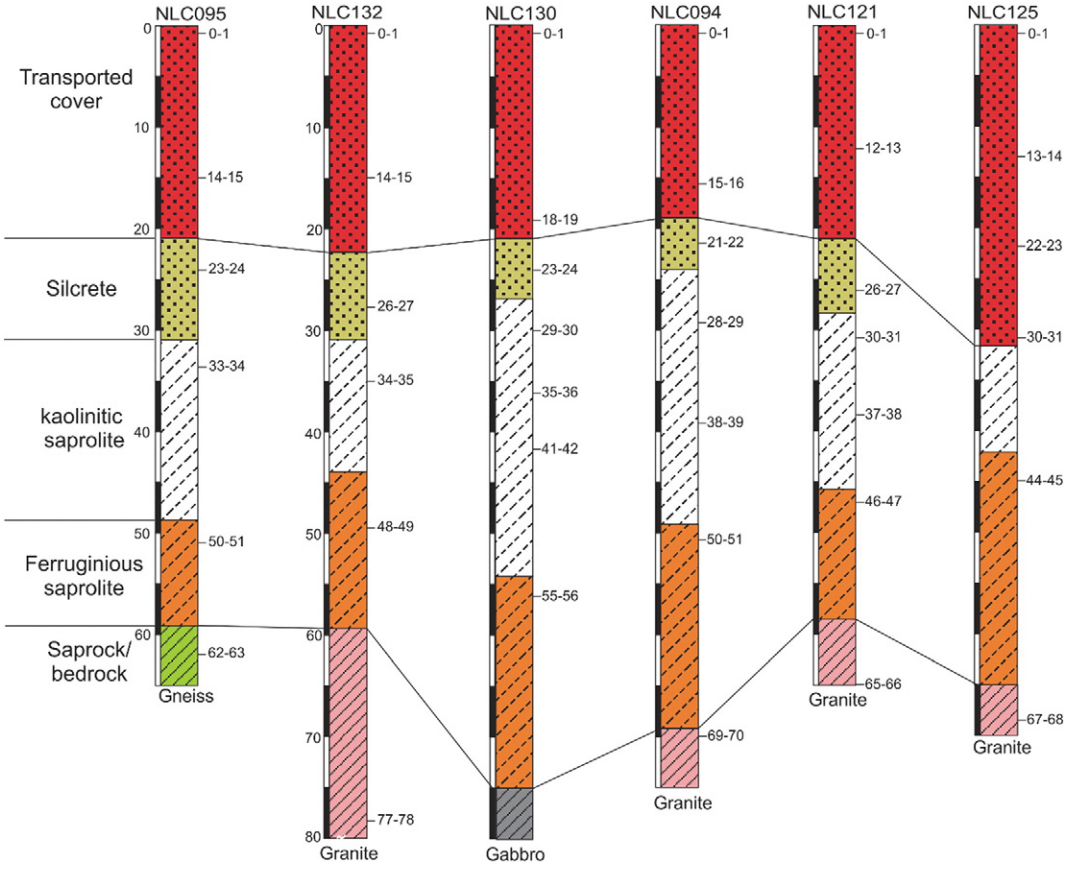

Fig. 2. Stratigraphy of transported and residual regolith at the Hercules site (Salama et al. 2016–same issue).

proxy to discriminate whether the regolith consists of transported or residual material (e.g. Cudahy, 1997; Anand and Paine, 2002). This model was successfully tested by Cudahy et al. (2005) to map transported versus in situ regolith for a 2500 km^2 area in the Kalgoorlie region of Western Australia using airborne hyperspectral imagery where poorly ordered kaolin was interpreted to be characteristic for transported materials whereas well ordered kaolin equates to saprock and saprolite developed over felsic and mafic bedrock. The resultant airborne kaolin crystallinity map was validated using visible and infrared reflectance spectrometric and XRD analyses of field samples.

Currently available satellite based systems only feature multispectral resolution and only in ASTER the position of the collected bands is designed to separate clay mineral groups from other hydrated silicates and carbonates (Laukamp et al., 2013b), which is in contrast to other satellite based remote sensing systems, such as the Landsat Thematic Mapper. A deconvolution of reflectance and emission spectra into distinct clay mineral species is therefore highly problematic. However, they can be used to map broad changes in mineral group information ranging from kaolinite to Al-rich smectites and white micas (e.g. beidellite, paragonite, muscovite) versus areas dominated by Al-poor smectites and white micas (e.g. montmorillonite, phengite) (Cudahy, 2011). On a continental to regional scale, this in turn can help to characterise geological provinces and drainage systems (Laukamp et al., 2013a).

In addition to compositional differences of clay minerals, the abundance and type of iron oxides vary in different regolith environments (Anand and Paine, 2002). Goethite is a typical weathering product of a number of primary ferromagnesian and sulphide minerals, such as pyroxenes, amphibole, olivine and pyrite, and occurs in the saprolite, but also in the mottled and ferruginous duricrust zones at the top of the weathering profile. However, hematite is formed new in the ferruginous zone by dehydration of goethite in drier conditions above the water table or by dissolution of goethite and reprecipitation as hematite (Cornell and Schwertmann, 2003). Therefore, goethite is in general the dominant iron oxide in the lower weathering profile (i.e. ferruginous saprolite), whereas hematite is increasingly abundant in the upper weathering profile. Cudahy et al. (2005) used this mineralogical change to support regolith landform classifications based on the kaolinite crystallinity derived from airborne hyperspectral data. The ferric oxide abundance and hematite/goethite ratio can also be estimated using multispectral remote sensing data, such as ASTER (e.g. Duuring et al., 2012). Hyperspectral remote sensing (e.g. HyMap; Haest et al., 2013) and proximal sensing data (e.g. HyLogging™; Haest et al., 2012a, b) provide a more detailed picture when compared to multispectral ASTER data.

4. Methodology

4.1. Remote sensing

Visible and infrared spectroscopy (VIRS) is a non-invasive, optical sensing technique that uses the reflectance and/or emission "spectral signature" of a given material in the visible (0.39 to 0.75 μm) and infrared (0.75 to 1000 μm) part of the electromagnetic spectrum to determine, for example, its presence, abundance and composition. Depending on the wavelength region, the radiation penetrates the upper few microns or only reflects from the surface of the analysed material. In geological applications, only the top few microns are typically sensed, such that a link between surface and sub-surface mineralogy and related processes is required. For example, in the Kalgoorlie area, unmapped ultramafic rocks kilometres in extent but covered by deep a weathering profile and related soil were mapped for the first time using airborne hyperspectral imagery based on detection of talc which persists from fresh rock to the surface (Cudahy et al., 2005).

The Advanced Spaceborne Thermal Emission and Reflection Radiometer (ASTER; Yamaguchi et al., 1999) collects 14 spectral bands in the visible-near (VNIR; 0.39 to ca. 1 μm), shortwave (SWIR; 1 to 2.5 μm) and thermal infrared (TIR; 6 to 14.5 μm), which are positioned in "atmospheric windows" to minimise the impact of atmospheric effects, such as atmospheric water or aerosols. The spatial resolution is 15 m/pixel in the VNIR, 30 m/pixel in the SWIR and 90 m/pixel in the TIR with a total swath width of about 60 km for all wavelength regions. The multispectral ASTER data can only be used to identify the abundance and the composition of mineral groups (Hewson et al., 2005; Ninomiya et al., 2005).

ASTER has been used for geological mapping (e.g. Ninomiya et al., 2005) at regional to prospect scales (Rowan et al., 2003; Cudahy et al., 2005, 2008; Ducart et al., 2006; Hewson and Cudahy, 2010; Witt et al., 2013), though few have considered the potential for specifically characterising the regolith (e.g. Hewson et al., 2005).

In the present study, selected precompetitive ASTER Geoscience Products (Cudahy, 2011, 2012; Caccetta et al., 2013) were employed for the surface characterisation of rock-forming minerals (Table 1). All selected ASTER maps were evaluated for potential impact of factors compromising mineral characterisation, such as green vegetation. These publically available ASTER Geoscience Products comprise 14 mineral group content and composition maps, such as the AlOH group mineral maps, which show the relative abundance and composition of major Al-bearing clay minerals (i.e. kaolinite group, Al-smectites, white micas), as well as a green vegetation and a false colour image.

4.2. HyLogging™

HyLogging™, designed by the CSIRO, enables rapid acquisition of reflectance spectra from drill cores, which can then be processed to generate detailed mineralogical information. The HyLogging™ system comprises a computer-controlled X–Y translation table moving in a serpentine path under a fixed-position spectrometer and illumination system to log contiguous reflectance spectra across the VNIR, SWIR and TIR. High resolution visible colour images (0.1 mm resolution) of the drill core were also collected during this process using a line-scan camera. The reflectance spectra were resampled to 8 nm spectral resolution and 1 cm spatial resolution in The Spectral Geologist software (TSG™).

Using TIR HyLogging™ data, Cudahy et al. (2009) successfully showed how to map the abundance and composition of feldspars, carbonates and quartz associated with hydrothermal alteration related to formation of Archaean Au deposits in the Eastern Goldfields of Western Australia. Tappert et al. (2013) used SWIR HyLogging™ data to characterise hydrothermal alteration in the Olympic Dam deposit, South Australia. The usefulness of HyLogging™ for exploration and resource modelling in regolith systems was shown by Haest et al. (2012a,b), who interpreted the abundance and composition of various iron oxide and clay mineral phases of a Tertiary Channel Iron Deposit (CID) in the Hamersley Basin Province.

Seven diamond drill cores and two reverse circulation (RC) drill holes from the study area (see Fig. 1c for location of diamond drill cores) were scanned using a HyLogging™ 3 system at the Core Library of the Geological Survey of Western Australia (GSWA), in Carlisle, Western Australia. The total amount of hyperspectral drill core data comprised about 70,000 VNIR, SWIR and TIR spectra collected from about 700 m drill core. Drill cores NLD097 and NLD210 are from the Hercules site, whereas the five remaining drill cores (NLD046, NLD069, NLD070, NLD071, NLD080) were collected from the Atlantis site. RC drill holes NLC071 and NLC094 are twin drill holes adjacent to NLD071 and NLD210, respectively.

Interpretation of the hyperspectral reflectance spectra was done using the Multiple Feature Extraction Method (MFEM, Cudahy et al., 2008; Laukamp et al., 2010). More specifically, the following MFEM scripts were used: 1) Ferric oxide abundance and Ferric oxide composition index (also called hematite/goethite ratio; cf. Haest et al., 2012a,b); 2) Kaolin abundance and crystallinity index (cf. Sonntag et al., 2012); 3) White mica abundance and composition index (further developed on the base of Sonntag et al., 2012, using the methods detailed in

Table 1
Selected mineral maps of the 2011 precompetitive WA ASTER Geoscience Products (Cudahy, 2011). A rainbow colour look up table was applied to all mineral group content and composition products. In the mineral group content yellow to red colours indicate a high relative content of the respective mineral group. For full table with detailed explanations of applied masks see Cudahy (2011).

Geoscience Product	Base algorithm	Material/ mineral group (examples)	References
False colour RGB	Red: b3, Green: b2, Blue: b1	Red = green vegetation	Cudahy et al. (2008)
Ferric oxide content	b4/b3	Hematite, goethite, jarosite	Cudahy et al. (2008)
Ferric oxide composition	b2/b1	Blue is goethite-rich, green is hematite-goethite, red/yellow is hematite-rich	Cudahy et al. (2008)
AlOH group content	(b5 + b7)/b6	Phengite, muscovite, paragonite, lepidolite, illite, brammalite, montmorillonite, beidellite, kaolinite, dickite	Rowan et al. (2003)
AlOH group composition	b5/b7	Blue is well crystalline kaolinite, Al-rich muscovite/illite, paragonite, pyrophyllite; Red is Al-poor (Si-rich) muscovite (phengite)	Cudahy et al. (2008)
MgOH/carbonate group content	(b6 + b9)/(b7 + b8)	Calcite, dolomite, magnesite, chlorite, epidote, amphibole, talc, serpentine	Cudahy et al. (2008)
MgOH/Carbonate group composition	b7/b8	Blue-cyan is magnesite, dolomite, amphibole, chlorite; Red is calcite, epidote, amphibole	Cudahy et al. (2008)
Ferrous iron in MgOH/carbonate index	b5/b4	Blue is low ferrous iron content in carbonate and MgOH minerals like talc and tremolite; Red is high ferrous iron content in carbonate and MgOH minerals like chlorite and actinolite.	Cudahy et al. (2008)
FeOH group content	(b6 + b8)/b7	Chlorite, epidote, jarosite, nontronite, gibbsite, gypsum, opal-chalcedony	Cudahy et al. (2008)
Green vegetation content	b3/b2	Vegetation	Cudahy et al. (2008)

Rodger et al., 2012). The Quartz abundance index is based on the relative depth of the 8.626 μm Reststrahlen feature for which the continuum is removed between 8.565 and 8.705 μm, determined using a 3 band polynomial fit around the band with the lowest reflectance.

4.3. X-ray diffraction (XRD)

Thirty nine powder samples from RC drill holes NLC094, NLC095, NLC121, NLC125, NLC130 and NLC132, were analysed using X-ray diffractometry (XRD) to determine the bulk mineralogical composition. The XRD data were collected using a Bruker D4 Endeavour AXS instrument operating with Co source radiation. The X-ray diffractogram patterns were collected from 5° to 90° 2θ, with increment of 0.02° and scan speed of 0.1° per second. Interpretation of the obtained XRD spectra was performed using the software package DIFFRAC.EVA and X-Plot. After identification of all mineral species present in each sample and fitting of the major peaks, a semi-quantitative interpretation was undertaken based on the XRD pattern's relative height and I/I_{cor} values. I/I_{cor} represents the ratio between the intensities of the strongest line of the compound of interest and the strongest line of corundum in a 50/50 mixture. I/I_{cor} values of the software internal structure database were used for semi-quantitative analysis. The quality of the results is heavily dependent on the visual adjustment of the y-scale values of each XRD pattern. Furthermore, the method assumes that the peak height is proportional to the net area of the peak, which may vary for different minerals, decreasing the accuracy of the results.

4.4. FTIR

Reflectance spectra of the 39 powder samples prepared for XRD were measured with a Bruker Vertex 70 Fourier Transform Infrared (FTIR) Spectrometer, where samples were placed in a black cup holder at the base of a gold Bruker Integrating Sphere 562-G for measuring directional hemispherical reflectance. To acquire the wavelength range between 1.450 and 16.5 μm, a liquid nitrogen cooled MCT detector was used with a KBr beam-splitter and a SiC Globar light source at a scanner velocity of 10 kHz. Sample and background scans were averaged over 256 scans. Interpretation of the obtained FTIR spectra was performed in The Spectral Geologist Software (TSG™).

5. Results

5.1. Reverse circulation drill hole data — XRD and FTIR

HyLogging™ data validation comprised further analyses of 39 rock chip samples from RC drill holes in the study area that were investigated by Salama et al. (2016–in this issue). Profiles of the six drill holes and locations of samples are shown in Fig. 2. The four major horizons displayed in the profile, are from bottom to top: 1) saprock (including gneiss, granite, granodiorite, dolerite and gabbro); 2) lower ferruginous and upper kaolinitic saprolite; 3) silcrete; and 4) transported cover. Results of the XRD and FTIR analyses of the 39 samples are shown in Table 2, which presents the four horizons in different shades of grey and white.

5.1.1. Saprock

According to the XRD results, the saprock materials are in general characterised by the presence of white mica and various amounts of other primary (i.e. pre-weathering) minerals, such as chlorite, feldspar and amphibole. From the FTIR spectra, white micas in the saprock are generally of a phengitic composition. The XRD estimated amounts of quartz are highly variable, ranging from traces to more than 80%. The great variation of mineral assemblages recorded by the XRD data can be assigned to the various rock types that were encountered in the saprock as indicated in Fig. 2. Also the FTIR data show a great variability in quartz abundance. However, there is a poor correlation between the detection of quartz by means of XRD and FTIR. This can be explained by the fact that the rock chip samples were milled to powder size for XRD and FTIR analyses, which caused complicating scattering effects in the acquired FTIR data. That is, the quartz reststrahlen features becomes subdued and even lost when particle size decreases <250 μm (e.g. Salisbury and Wald, 1992). However, quartz is also recognised in some samples by FTIR but not by XRD, such as NLC130_15. It should be noted that reflectance spectra acquired from solid drill core are less affected by these complicated scattering effects.

In some deeper drill holes, such as NLC130, NLC132, kaolinite is found throughout the drill holes including the bottom saprock, which shows the deep weathering front. In contrast, other drill holes show less intense weathering, such as NLC94, NLC121 and NLC130, where FTIR SWIR and midwave infrared (MIR) spectra indicate kaolinite only at the top of saprock. This may be due to a greater sensitivity of XRD for detection of kaolinite when compared to reflectance spectroscopy in the investigated sample material. Iron oxides are present as goethites in the lowermost samples of NLC094, NLC130 and NLC095.

5.1.2. Saprolite

XRD results for the saprolite (mid grey — Table 2) show that quartz is generally dominant, with lesser, highly variable amounts of white mica, amphibole and feldspar. Kaolinite is also evident in the XRD as a minor component. FTIR data indicate well crystalline kaolinite for the saprolite in almost all drill holes, which is exemplified by the characteristic spectral signature of sample 94_04 (Fig. 3).

Table 2
XRD & FTIR results.

				XRD						FTIR	
	from	to			kaolin	white					kaolin
sample Nr	[m]	[m]	RH	quartz	group	mica	chl	fsp	amph	quartz	group
NLC95_34	0	1	A	+++	trace	–	–	–	–	Y	Y (px)
NLC95_35	14	15	A	+++	o	–	–	–	–	Y	Y (px)
NLC95_36	23	24	B	+++	–	–	–	–	–	Y	Y (px)
NLC95_37	33	34	C	++	+	o	–	–	–	?	Y (wx)
NLC95_38	50	51	C	o	trace	+	–	Y	–	Y	–
NLC95_39	62	63	D	o	–	+	Y	–	Y	Y	–
NLC132_22	0	1	A	trace	trace	+	–	Y	Y	Y	Y (px)
NLC132_23	14	15	A	+++	trace	–	–	–	–	Y	Y (px)
NLC132_24	26	27	B	+++	o	–	–	–	–	Y	Y (px)
NLC132_25	34	35	C	++	+	o	–	–	–	Y	Y (wx)
NLC132_26	48	49	C	++	++	o	–	–	–	–	–
NLC132_27	77	78	D	o	o	+	–	Y	–	–	–
NLC130_15	0	1	A	o	–	+	–	Y	Y	Y	Y (px)
NLC130_16	18	19	A	o	–	+	–	Y	Y	Y	Y (px)
NLC130_17	22	23	B	+++	trace	–	–	–	–	Y	Y (px)
NLC130_18	29	30	C	+++	trace	–	–	–	–	?	Y (wx)
NLC130_19	35	36	C	+++	trace	–	–	–	–	–	Y (wx)
NLC130_20	41	42	C	+	++	o	–	–	–	?	Y (wx)
NLC130_21	55	56	C	+	o	+	–	–	–	–	–
NLC94_01	0	1	A	o	o	+	–	Y	Y	Y	Y (px)
NLC94_02	15	16	A	o	trace	+	Y	Y	Y	Y	Y (px)
NLC94_03b	21	22	B	+++	–	–	–	–	–	Y	?
NLC94_04	28	29	C	+++	o	–	–	–	–	?	Y (wx)
NLC94_05	38	39	C	+++	–	–	–	–	–	Y	Y (wx)
NLC94_06	50	51	C	++	+	+	–	–	–	?	–
NLC94_07	69	70	D	trace	–	+	–	Y	Y	–	–
NLC121_08	0	1	A	trace	–	o	Y	Y	Y	Y	Y (px)
NLC121_09	12	13	A	+++	trace	–	–	–	–	Y	Y (px)
NLC121_10	26	27	B	+++	o	–	–	–	–	Y	Y (wx)
NLC121_11	30	31	C	+++	o	–	–	–	–	–	Y (wx)
NLC121_12	37	38	C	++	trace	+	–	–	–	?	Y (wx)
NLC121_13	46	47	C	trace	–	o	–	Y	Y	?	–
NLC121_14	65	66	D	++	–	o	Y	–	Y	?	–
NLC125_28	0	1	A	+++	trace	–	–	–	–	Y	Y (px)
NLC125_29	13	14	A	+++	o	–	–	–	–	Y	Y (px)
NLC125_30	22	23	A	+++	trace	–	–	–	–	Y	Y (px)
NLC125_31	30	31	A	++	o	++	–	–	–	?	Y (px)
NLC125_32	45	46	C	+++	–	o	–	–	Y	–	–
NLC125_33	67	68	D	+++	o	–	–	–	–	Y	–

Mineral abundance: +++ — major (>80%); ++ — very common (40–80%); + — common (20–40%); o — minor (5–20%); trace (1–5%); – — absent (0%); Y — present (not quantified); ? — questionable; px — poorly crystalline; wx — well crystalline. Different regolith horizons are shown by shades of grey and white: white — transported cover; grey 1 — silcrete; grey 2 — upper kaolinitic and lower ferrugnieous saprolite; grey 3 — saprock (i.e. gneiss, granite, granodiorite, dolerite, gabbro).

5.1.3. Silcrete

The silcrete layer is generally characterised by very high amounts of quartz with traces to minor amounts of kaolinite (light grey — Table 2). The FTIR results show kaolinite in most of the RC holes, with the kaolin crystallinity changing from well crystalline in saprolite to poorly crystalline kaolinite in the silcrete layer.

5.1.4. Transported cover

XRD results for the transported cover are highly variable (white — Table 2). The quartz content ranges from trace amounts to more than 80% and a number of primary minerals can be present. White mica, for example, can constitute up to 32% in the transported cover. In NLC94, white mica contents reach 26% and chlorite, amphibole and feldspar are present. According to XRD, kaolinite can be absent or be present in trace amounts or as a minor component. However, FTIR data suggest the presence of poorly crystalline kaolinite in all samples classified as transported cover. Based on the XRD data, iron oxides are evident in the transported cover horizon of drill holes NLC094, NLC121 and NLC130.

5.1.5. Kaolinite crystallinity

Fig. 3 shows reflectance spectra of all seven samples from drill hole NLC94, where, in the top five samples, hydroxyl-related stretching fundamentals in the MIR between 2705 and 2761 nm can be assigned to kaolinite. SWIR reflectance spectra of the same samples indicate that kaolinite is also present in samples 94_01, 94_02, 94_04 and 94_05. A low ratio of the reflectance of the shorter wavelength combination band of the outer hydroxyl group in the octahedral layer of kaolinite at 2160 nm versus the combination band of the inner hydroxyl group at 2206 nm is evident in samples 94_04 and 94_05, which are located in the upper kaolinitic saprolite. This suggests a well crystalline kaolinite when compared to the uppermost samples 94_01 and 94_02 sourced from the transported cover, which have a high band ratio and hence can be classified as poorly crystalline kaolinite (cf. Cudahy, 1997). The transition from well crystalline kaolinite in the saprock and saprolite to poorly ordered saprolite in the transported cover can be observed in all but one of the RC drill holes (i.e. NLC125), where only poorly crystalline kaolinite is recorded (Table 2). Fig. 4a shows the kaolin abundance and crystallinity index (sensu Cudahy et al., 2008) extracted from the FTIR reflectance spectra that were acquired from the all RC drill holes, coloured by the regolith classification according to Salama et al. (2016–in this issue, Fig. 2). The kaolin crystallinity values are high for the kaolinitic saprolite when compared to the transported cover. The kaolin crystallinity index is based on the relative depth of the combination bands of the outer hydroxyl groups in kaolinite (R2159/R2180, Fig. 4b), which changes according to the order of the kaolinite structure (Cudahy, 1997). The kaolin abundance and crystallinity indices were also applied to HyLogging™ data acquired from RC drill hole and diamond drill core data, showing the applicability of this parameter to data acquired using different hyperspectral technologies and different sample media.

5.2. Reverse circulation drill hole — HyLogging™ data

HyLogging™ data acquired from the available regolith sample set of NLC094 (24 samples) provide a spatially more detailed view over the mineralogical changes from the saprolite to the transported cover. SWIR absorption features in the 2150 to 2450 nm wavelength region can all be assigned to hydroxyl related combination bands in silicate minerals (Fig. 5). For an overview of the here summarised absorption features assigned to their respective minerals see Laukamp (2011) and Laukamp et al. (2012). The lowermost saprolite sample at 25.5 m contains white mica of phengitic composition (i.e. $\nu+\delta$Al–O–H at 2223 nm) as well as amphibole, whereas the upper saprolite sample at 21.5 m contains amphibole and possibly another Fe/Mg-bearing sheet silicate, such as chlorite. Samples at 17.5 m and 16.5 m are characterised by white mica and Fe/Mg-bearing sheet silicate, such as Fe-smectites. SWIR reflectance signatures of the top four samples in the transported cover are dominated by the presence of kaolinite, which is well crystalline in samples at 15.5 m and 14.5 m and poorly crystalline in samples at 6.5 m and 2.5 m. The latter trend of well crystalline kaolinite at the bottom to poorly crystalline kaolinite at the top confirms

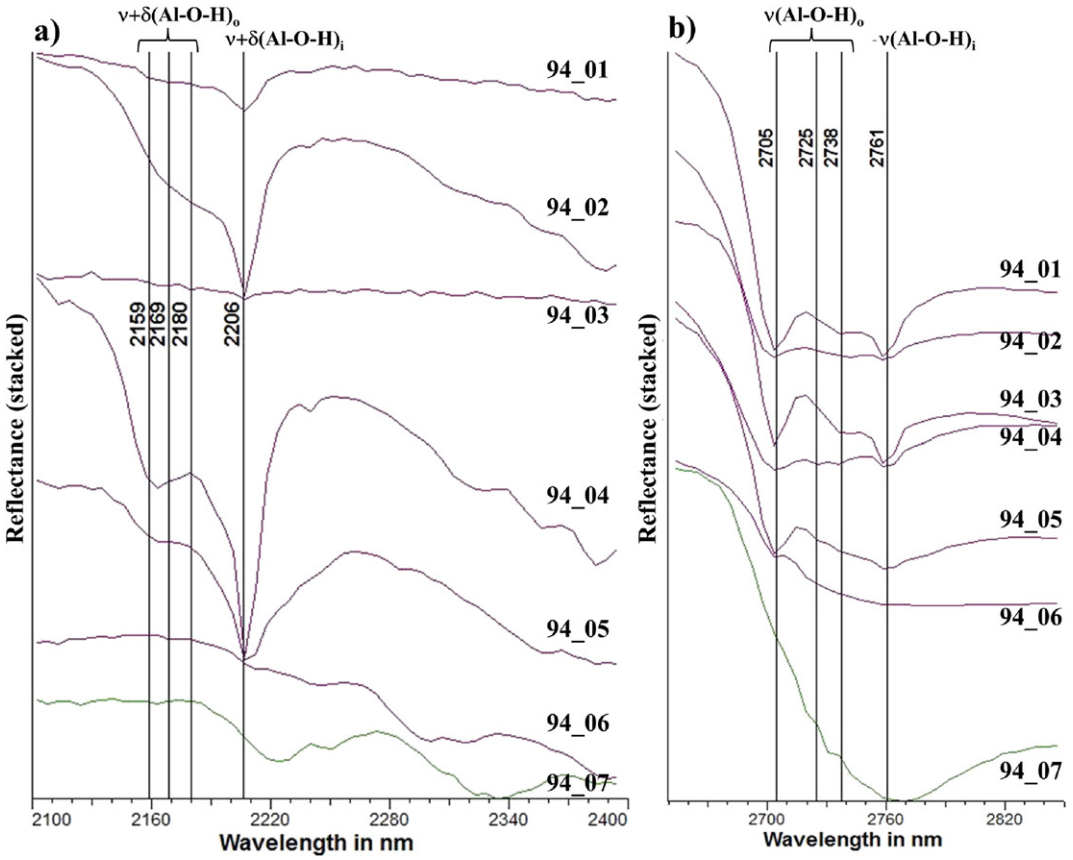

Fig. 3. FTIR reflectance spectra of selected samples from NLC094: a) SWIR; b) MIR. Wavelength positions of absorption features related to the stretching vibrations (ν(Al–O–H)) and combination bands ($\nu+\delta$(Al–O–H)) of the inner and outer hydroxyl groups of kaolinite are shown next to the vertical lines.

observation from the FTIR data presented above and was also described by Salama et al. (2016–in this issue).

Electronic absorption features in the VNIR can be largely assigned to ferrous and ferric iron in silicate and iron oxide minerals. The two saprolite samples of NLC094 show a distinct slope from about 1600 nm towards shorter wavelengths, indicating the presence of ferrous iron that is possibly contained in amphiboles observed in the SWIR of the same samples. The top six samples acquired from the transported cover show only ferric oxide features. The prominent ferric iron crystal field absorption feature at around 900 nm shifts from 955 to 895 nm from the bottom sample of the transported cover to the top, indicating goethite as the dominating iron oxide in the lower part and hematite in the upper part of the drill hole. The same trend was observed in NLC071, where goethite is the dominating iron oxide at around 7.5 m depth, changing into hematite at the top. This trend was not recognisable from the XRD samples presented above.

5.3. Drill core HyLogging™ data

5.3.1. HyLogging™ of regolith

Contiguous HyLogging™ data acquired from NLD210, which is the twin drill core to RC drill hole NLC094, recorded all in situ regolith horizons. Drill cores NLD071 and NLD080 feature intensely weathered bed rock in the upper metres of the scanned intervals (boundary at ca. 57 m and ca. 61 m respectively). Fig. 6 shows representative images of the various regolith horizons (Fig. 6a), the distribution of selected mineral groups and changes regards their composition or crystallinity interpreted from multiple feature extraction scripts (Fig. 6b to e), as well as VNIR–SWIR and TIR spectra representative of the regolith horizons.

The iron oxide abundance and composition (Fig. 6b), the kaolinite abundance and crystallinity (Fig. 6c), the white mica abundance (Fig. 6d) and the quartz abundance (Fig. 6e) show distinct changes in the drill hole, which can be interpreted as single stratigraphic layers in the regolith described by Salama et al. (2016–in this issue) and that were observed in the regolith samples of NLC094. However, the HyLogging™ data of NLD210 provide an even greater detail of the regolith. The lower section of saprock is characterised by abundant white mica of phengitic composition (Fig. 6d), as well as other primary minerals, such as chlorite, and the absence of kaolinite (Fig. 6c). Towards the top of the saprock the amount of white micas decreases, whereas the abundance of kaolinite increases. Iron oxides and quartz are present throughout the saprock and show a very irregular pattern of abundance. The transition from saprock to saprolite at ca. 37 m is smooth with poorly crystalline kaolinite developing as a major component. The lower ferruginous saprolite is marked by elevated iron oxide abundance (Fig. 6a, f) and more consistent quartz abundance values (Fig. 6e). A high abundance of well crystalline kaolinite can be observed in the upper kaolinitic saprolite. White mica and iron oxides are virtually absent, whereas quartz continues to be present. Towards the transition zone with the silcrete at ca. 24.5 m depth, the kaolinite is poorly crystalline and white mica are present. The transition zone to the silcrete between 23 and 24.5 m contains quartz, white mica and iron oxides, but no kaolinite. The silcrete is characterised by very high quartz abundance with very characteristic TIR spectral signatures of quartz (Fig. 6g). SWIR spectral signatures suggest the presence of Opaline silica (Fig. 6f). However, the silcrete contains layers with abundant iron oxides and/or largely poorly crystalline kaolinite.

Most of the investigated diamond drill core data show changes in the abundance and/or composition of certain mineral groups towards the

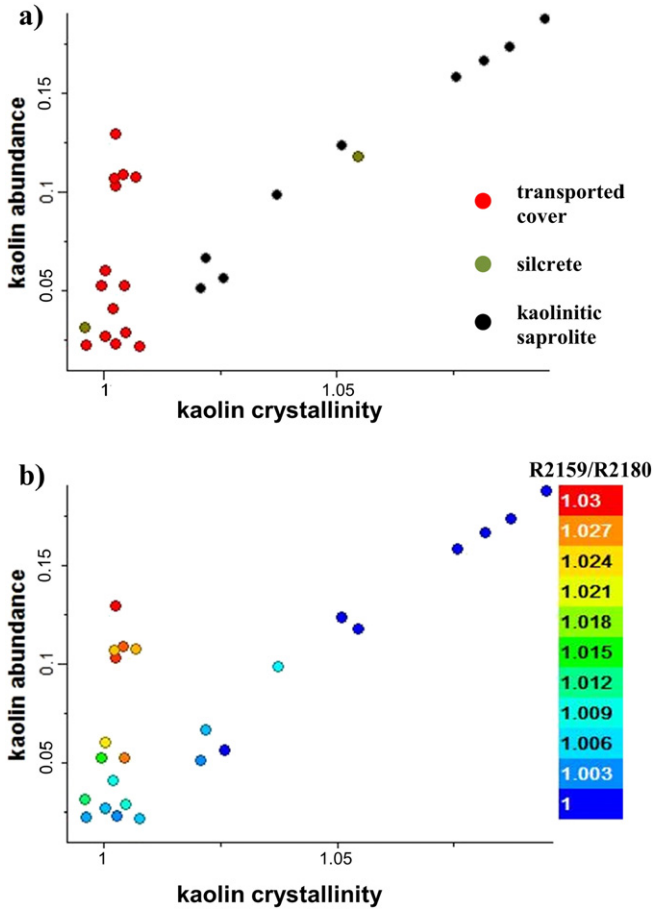

Fig. 4. Kaolin abundance and crystallinity index (sensu Cudahy, 1997; Sonntag et al., 2012) extracted from FTIR reflectance spectra acquired from all RC drill holes coloured by a) the regolith classification according to Salama et al. (2016–in this issue) and b) the ratio of the reflectance values at 2159 and 2180 nm (R2159/R2180).

top of the drill hole that are possibly related to a weathering overprint. The iron oxide abundance, for example, is in almost every drill core distinctly increasing in the upper parts (e.g. NLD046, from 179 m upwards; NLD210, from 90 m upwards).

5.3.2. HyLogging™ of bedrock lithologies:

Four major bedrock lithologies can be observed at the Hercules and Atlantis sites and were correlated in the seven diamond drill cores using the HyLogging™ data. The lithologies are from bottom to top: 1) granitoids and granofels, 2) two mica schists, 3) quartz-mica schists and 4) intermediate intrusives.

Lithological and mineralogical variations in granitoids and granofels from drill core NLD210 are representative for the other drill core data and are used as a base for more detailed descriptions in the following. The lower parts of drill core NLD210 comprise a comparably uniform granofels that is, in distinct layers, highly chertified and affected by intense sericite-epidote alteration at around 80 m. The plagioclase content is overall higher in NLD210 when compared to NLD097. The white mica composition shows in general more Al-poor micas in NLD210, which is similar to other lithologies in drill cores of the Atlantis site (Fig. 2). All drill cores intersecting the granitoid and granofels units exhibit a distinct horizon that is characterised by 1) increasing sericitisation and/or chlorite/biotite alteration towards its centre, 2) increased carbonate alteration at its rims and 3) distinct changes in the white mica composition when compared to the surrounding rocks. In NLD210, this alteration zone shows a distinct epidote alteration towards its centre. In NLD210, silicified horizons are located at around 115 m, 127.5 m and from 166 to 169 m. Similar to cherts in other drill cores a decrease or lack of amphibole abundance can be observed (not shown here). However, in contrast to the other cherts, silicified layers in NLD210 are characterised by distinct carbonate content and, especially in case of the lower silicified unit at around 166.5 m, by a decrease in white mica abundance.

Two-mica schists and quartz sericite schists only occur at the Atlantis site, showing a highly variable amount of di- and tri-octahedral sheet silicates and vein- or breccia style carbonate alteration. Distinct amphibole-rich intervals could point towards mafic igneous rocks comparable with amphibole-rich intrusives in the upper parts of the drill cores at the Atlantis site.

5.4. Remote sensing data

5.4.1. ASTER

A False Colour RGB ASTER image draped over a DEM of the study area (Fig. 7) provides some basic information about some of the regolith landforms in this area. In comparison with Fig. 1b, three distinct domains can be inferred from the False Colour RGB: 1) erosional regime with drainage systems (example location indicated by red arrow), 2) flat depositional regime (black arrow, NLD046, NLD210), and 3) dune fields northwest of a northeast trending barrier. The northern and eastern parts of the study area are heavily impacted by fire scars (e.g. to the northeast of NLD210).

Comparison of the False Colour RGB with the surface geological map (Fig. 1b) shows a major difference in the distribution of the dune fields. That is, large parts of the Hercules area are mapped as Quaternary dune fields in the surface geological map, whereas the False Colour RGB suggests that the dune fields are restricted to the area north of the Neale and Hercules sites. The DEM of the Hercules area (Gallant et al., 2011; Fig. 1c) indicates that this area is elevated compared to the lower lying area to the southwest of a northeast trending morphological boundary.

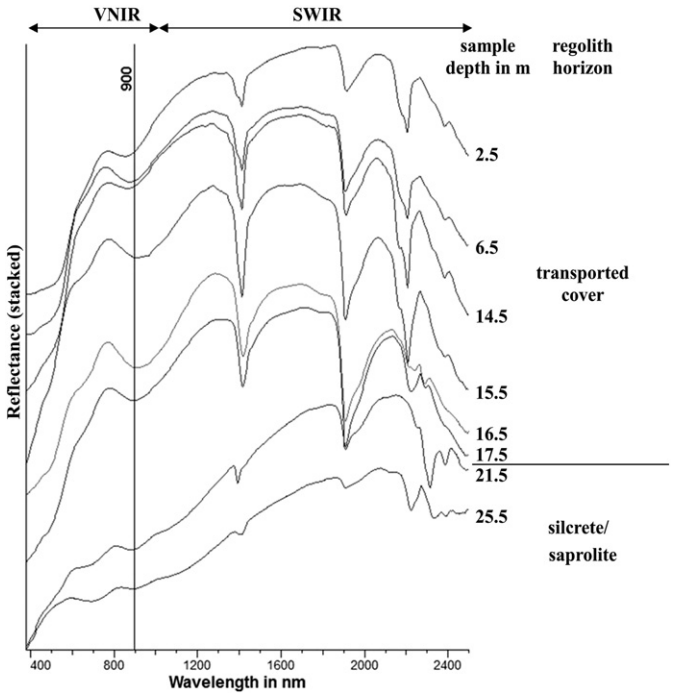

Fig. 5. HyLogging™ VNIR–SWIR reflectance spectra of selected samples from NLC094.

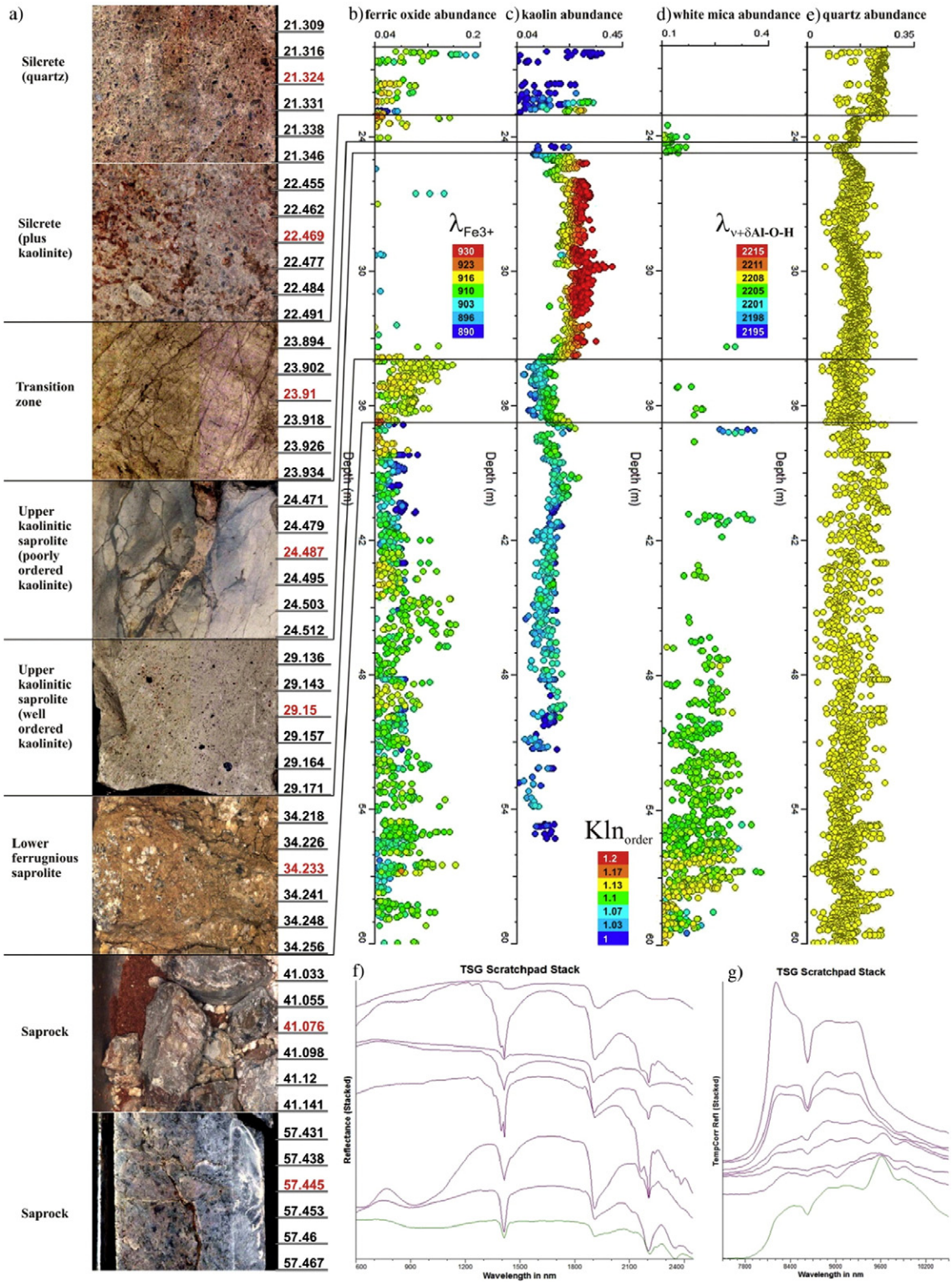

Fig. 6. HyLogging™ data from drill core NLD210 (20 to 60 m depth): a) Stacked line scan images of main regolith horizons; b) ferric oxide abundance coloured by wavelength position of the ferric iron absorption feature at around 900 nm; c) kaolin group abundance and composition; d) white mica abundance and composition; e) quartz abundance index; f) stacked VNIR–SWIR reflectance spectra of sample intervals marked in red in a); g) corresponding TIR spectra.

The regolith stratigraphy of the study area, especially mapping residual–erosional–depositional landforms, was interpreted using the spectral-mineralogical model presented in Table 3. Critical ASTER products for this purpose include: 1) AlOH Group Content, 2) AlOH Group Composition Fig. 7b), 3) Ferric Oxide Content (Fig. 7c), and 4) Ferric Oxide Composition (Fig. 7d) with diagnostic attributes described in Table 4. A new regolith map (Fig. 8) was then generated using these ASTER Geoscience Products which helped the development of new schematic regolith landform model for the northeastern Albany–Fraser Orogen (Fig. 9).

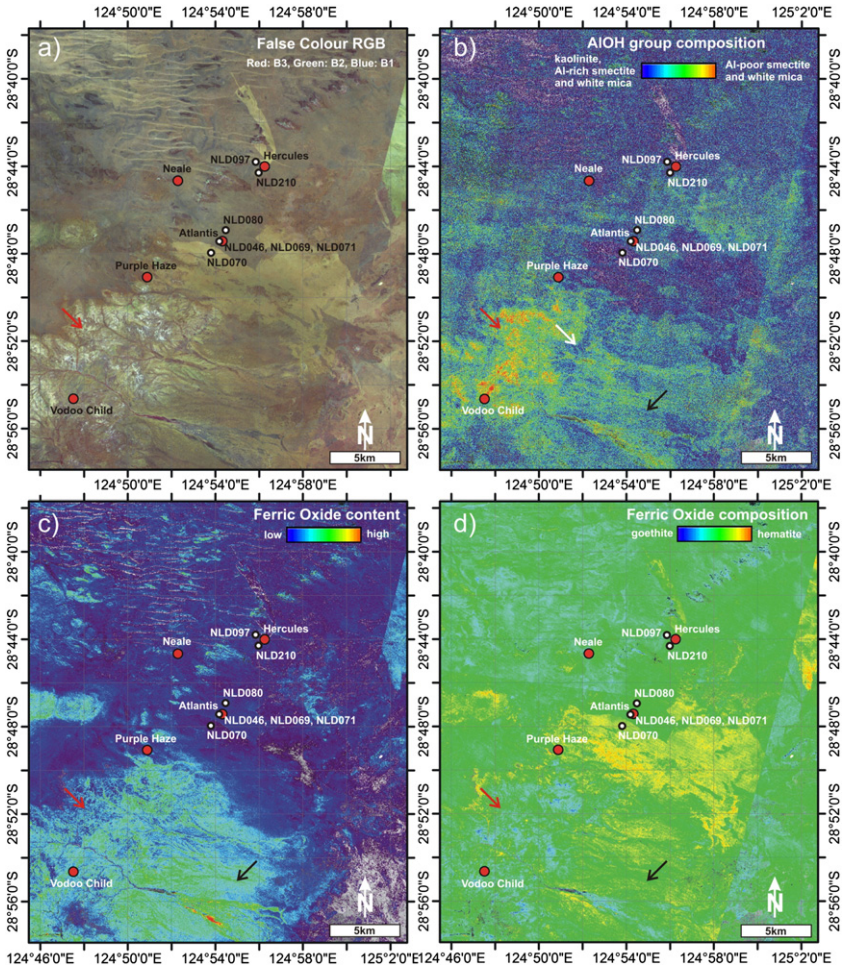

Fig. 7. ASTER Geoscience Products (Cudahy, 2011) of the study area with locations of Neale, Hercules, Atlantis, Purple Haze and Vodoo Child sites, and hylogged drill cores NLD046 and NLD210: a) False Colour RGB; b) AlOH Group composition; c) Ferric Oxide Content; d) Ferric Oxide Composition. See Table 1 for description of respective ASTER Geoscience Products. Red arrow: erosional regime; white arrow: kaolinite-rich fringe around erosional regime; black arrow: depositional regime (for further explanations please see text.

5.4.2. Erosional regime

The erosional regime comprises exposed "saprolite and bedrock-dominated terrains" (SP). The surface geological map shows outcrops of Proterozoic metasedimentary/—volcanic rocks and granites, as well as Mesozoic sediments of the Madura Formation and Permian glacial sediments of the Paterson Formation in the erosional regime (Fig. 1b). These areas typically show an ASTER response of warmer colours in the AlOH Group composition (Fig. 7b, red arrow), i.e. Al-clays that are poor in kaolin but rich in white mica or Al-smectite (e.g. montmorillonite). This highlights areas of weathered Proterozoic bedrock (SP_P) and silcrete (SP_M). From the Hylogging™ data, these warmer ASTER AlOH Group composition responses equate to phengitic white mica in the bedrock and saprolite (Fig. 6). The upper saprolite (SP_F) contains abundant kaolinite, which is evident in the ASTER image as kaolin fringes around areas of exposed bedrock or lower saprolite (white arrow in Fig. 7b) and is confirmed by the drill hole data (Fig. 6). The ASTER Ferric Oxide content product (Fig. 7c) shows considerable variability across the interpreted erosional regime (Fig. 1b). Exposed bedrock generally shows intermediate to high iron oxide abundance, with areas mapped as Paterson Formation in Fig. 1b in the northeast showing the highest contents, especially where they form mesas (white arrow in Fig. 7c).

Goethite is the dominating iron oxide type in the bedrock, as indicated by the blue colours in the Ferric Oxide composition image (red arrow in Fig. 7d). The ferruginous saprolite can be subdivided into a goethite-rich (SP_FG) and a hematite-rich (SP_F) endmember, with the latter one having, in general, a lower iron oxide content (Fig. 7c). Whereas the surface geological map (Fig. 1b) shows both Mesozoic and Proterozoic bedrocks in the southwest, the ASTER Geoscience Products imply a distinctly different mineralogical signature between the bedrock in the

Table 3
VNIR and SWIR active mineralogical factors for regolith landform classification in the Albany–Fraser Orogen.

Regolith landform	Mineral group factor			
	Al-clay group	Kaolin crystallinity	Iron oxide group	Primary minerals
SD — Sediment-dominated terrains (e.g. alluvial plains and dunes)	Kaolinite, smectite	Low	Hematite	atypical
GS — Sands, ferruginous gravels and duricrust-dominated terrains (levelled plateaus)	Kaolinite	Low or high	Hematite	atypical
SP — Saprolite and bedrock-dominated terrains (i.e. "breakaways")	Kaolinite, smectite, white mica	High	Goethite	Amphibole, chlorite, talc, white mica

Table 4
ASTER derived mineralogical factors for regolith landform classification in the Hercules area.

	Mineral group factor			
Regolith landform	Al-clay abundance	Al-clay group composition	Iron oxide abundance	Iron oxide group composition
SD — Sediment-dominated terrains (e.g. alluvial plains and dunes) — depositional landforms				
SD (undifferentiated)	Low–high	Kaolinite, smectite, white mica	Low–high	Goethite, hematite
SD_Dr (drainage)	Low	White mica, smectite	High	Goethite
SD_C (colluvium)	Low	Kaolinite, smectite, white mica	Intermediate–high	Goethite, hematite
SD_A (alluvium)	Low–high	Kaolinite, smectite	Low–intermediate	Goethite, hematite
SD_H (hardpan)	Intermediate–high	Kaolinite, smectite	Intermediate	Hematite
SD_Du (dunes)	Low–intermediate	Kaolinite, smectite	Low	Goethite
GS — Sands, ferruginous gravels and duricrust-dominated terrains (levelled plateaus) — relict landforms				
GS (undifferentiated)	Low	Kaolinite, smectite, white mica	Low	Goethite
SP — Saprolite and bedrock-dominated terrains (erosional, e.g. "breakaways") — erosional landforms				
SP (undifferentiated)	Low–high	Kaolinite, smectite, white mica	Low–high	Goethite, hematite
SP_F (ferruginous saprolite)	Low–high	Kaolinite, smectite	Low–intermediate	Hematite
SP_FG (ferruginous saprolite 2)	High	Kaolinite, smectite, white mica	Intermediate–high	Goethite
SP_P/M	Low–high	White mica, smectite	Intermediate–high	Goethite
SP_P (Proterozoic)	Intermediate–high	White mica, smectite	Intermediate–high	Goethite
SP_M (Mesozoic)	Low	White mica, smectite	High	Goethite

southwest (around the Voodoo Child and Purple Haze sites) and those in the northeast (between Neale and Hercules sites). All outcrops and related saprolites in the vicinity of the Neale and Hercules sites are tentatively assigned to Proterozoic bedrock.

5.4.3. Depositional regime

The surface geological map (Fig. 1b) divides the depositional area to the east of the northeast trending morphological boundary into dune fields in the north and colluvium in the south. The ASTER Geoscience Products support this subdivision, however, with a different position of the boundary (Fig. 8). Based on the ASTER Geoscience Products a more uniformly sediment-dominated terrain in the north can be distinguished from the highly separated, sediment-dominated terrain in the south, as described above. A comparison of the mineralogy in the two sediment-dominated terrains with possible source areas in the northwest imply that the transported material in the east was sourced from the northwestern dune fields, whereas the transported material in the southeast derived from the Proterozoic basement to the west.

When compared to the erosional regimes, the different depositional regimes (i.e. dune fields and sandplain depositional environment), show a different character in the ASTER Geoscience Products. The relative abundance of clay minerals can vary significantly between the different depositional environments (Table 4, Fig. 8). Low Al-clay abundances, dominated by Al-smectite and white mica, were observed in drainage systems (SD_Dr) and colluvium (SD_C), whereas alluvium (SD_A) and hardpans (SD_H) are both characterised by an intermediate to high abundance of kaolinite. The reason for the low Al-clay abundance in the drainage systems and the colluvium could be due to the erosional component of this regime. However, it should also be noted that in the AlOH Group Composition image (Fig. 7b), blue areas northeast

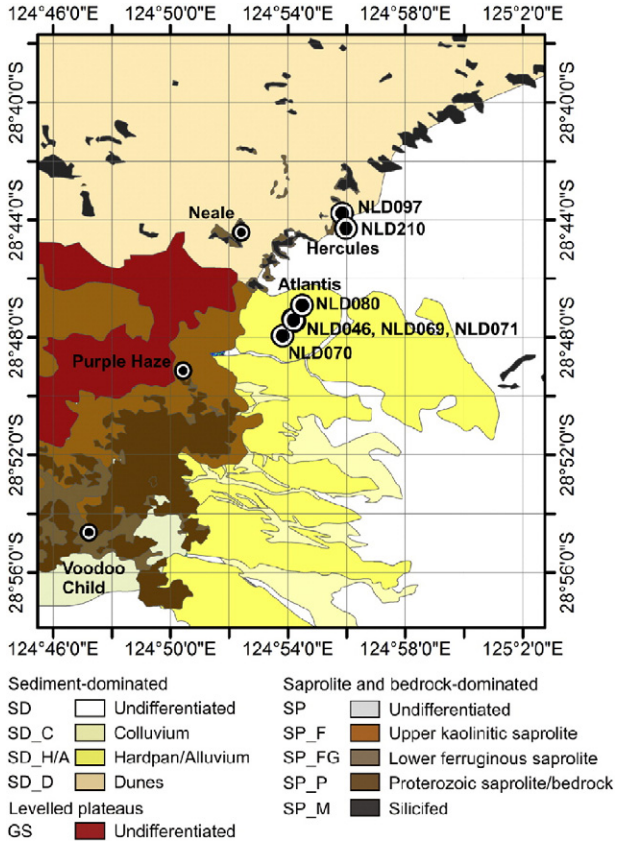

Fig. 8. Regolith landform map of the Neale and surrounding area, Albany–Fraser Orogen (Western Australia), inferred from HyLogging™ and ASTER remote sensing data. Locations of diamond drill cores investigated for this study shown as larger circles.

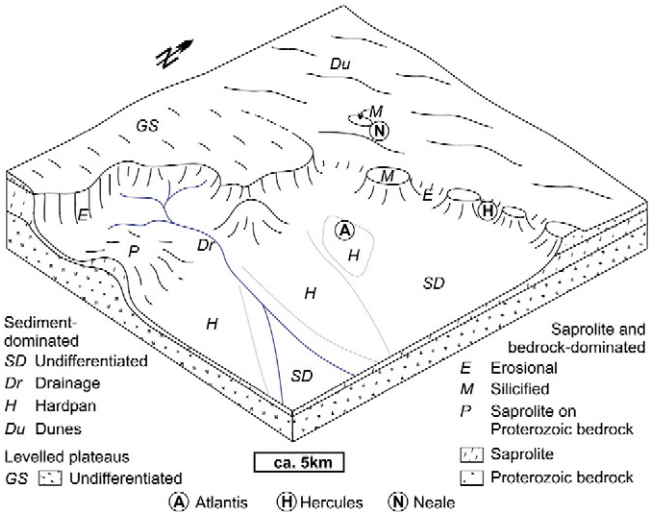

Fig. 9. Schematic regolith block model around the Hercules area, Albany–Fraser Orogen (Western Australia). Sediment-dominated (SD) terraines: Du — dunes, H — hardpan; Saprolite and bedrock-dominated (SP): M — Mesozoic, P — Proterozoic, E — erosional; Levelled plateaus (GS).

of the black arrow indicate fire scars, complicating the interpretation of the remote sensing data.

The abundance of iron oxides (Fig. 7c) in depositional regimes (SD_A, SD_H) is generally lower than in the depositional/erosional regimes (SD_Dr, SD_C). Hematite is the main iron oxide mineral in hardpans, compared to goethite dominating in drainage channels (Fig. 7d). The two regolith environments can be mapped in great detail when occurring in the same area (Fig. 8). Four drill holes at the Atlantis site are located in one of these hardpans. Only two of the drill holes from Atlantis (NLD070, NLD080) record HyLogging™ data from the lowermost regolith, represented by saprock, but all four drill holes show an increased iron oxide abundance towards the top of the core, which might be related to the formation of the hardpan. High abundance of low crystalline kaolinite in the upper metres of drill hole NLD080 (ca. 51 m depth) suggests input of material of a transported origin.

Dune fields (SD_Du) show low to intermediate Al-clay contents, mainly comprising kaolinite and possibly smectite according to the AlOH Composition image. This is in contrast to erosional features, which dissect this otherwise depositional environment and are characterised by high white mica and/or Al-smectite abundance and low kaolinite abundance. This enhances the possibility of mapping bedrock or saprolite (i.e. erosional features) in the dune fields. The resulting bedrock or saprolite domains are shown in Fig. 8. The dune fields north of the Neale and Hercules sites also show a low abundance of iron oxides (Fig. 7c), dominated by goethite (Fig. 7d), whereas other depositional areas southeast of the northeast trending morphological boundary contain relatively more iron oxides, often dominated by hematite (e.g. in hardpans, SD_H). The ASTER Geoscience Products suggest a more complex regolith subdivision of the depositional area than shown in the surface geological map (Fig. 1b; Stewart et al., 2008), where large areas are mapped as dune fields.

5.4.4. Relict landform

The third major regolith environment is represented by relict landforms, which comprise levelled plateaus that feature in the Yilgarn Craton regolith model, such as mainly sands, ferruginous gravels and duricrusts (Tables 1 and 3). In the Yilgarn Craton, this relict landform is characterised by an intermediate abundance of kaolinite, as well as low to high abundance of iron oxides, with hematite being the dominant iron oxide mineral (Laukamp, 2013). In relict landforms at Hercules though, the abundance of clay minerals is in general low and iron oxides are mainly of a goethite type (Fig. 7d). These observations set the relict landform apart from the surrounding erosional landforms (i.e. saprolite and bedrock dominated terrains) (Fig. 8). The transition of the newly mapped relict landform to the northern dune fields is very well defined in the ASTER Iron Oxide Content (Fig. 7c) and Opaques Index images (not shown here), with increased abundance of opaque material at erosional features dissecting the depositional landform of the dune fields. This mineralogical differentiation is not captured in the original surface geological map (Fig. 1b), where the same area is described as dunes and sandplains, stretching from west of the Purple Haze site to the north of the Neale and Hercules sites. However, the ASTER Geoscience Products clearly show mineralogical differences between these two areas.

6. Discussion

6.1. Subsurface data

Reflectance spectroscopic data were acquired from subsurface samples in the form of drill core and RC drill chips using the HyLogging™ system. In addition, selected RC samples were analysed with XRD and FTIR and compared with geochemical analyses described by Salama et al. (2016–in this issue) for validation of the reflectance data. All analyses support the existence of a regolith stratigraphy that basically can be separated in to saprock, saprolite, silcrete and a "top transported cover" horizon, which were then mapped with the ASTER Geoscience Products (Chapter 6.2 Surface data). Even though restricted to the Hercules and Neale sites, the Hylogging™ data and accompanying XRD and FTIR analyses provided detailed information about the mineral assemblages, that helped to understand the larger scale mineral footprints and regolith characteristics mapped by the remote sensing data.

6.1.1. Bedrock

Unweathered bedrock was only accessed by the HyLogging™ data acquired from drill cores, revealing four major bedrock lithologies in the study area. These are 1) granitoids and granofels, 2) two-mica schists (only at Atlantis), 3) quartz-mica schists and 4) intermediate intrusive and granitoids. Noteworthy mineralogical characteristics are the predominantly phengitic composition of white micas in all bedrock intervals as well as distinct amphibole-rich intervals, which could point to mafic intrusions.

6.1.2. Saprock

Saprock was intersected by the diamond drill core and RC drill holes. Primary minerals are evident from XRD of samples from the lower saprolite (Table 2). Apart from white mica the occurrence of the single primary mineral phases inferred from XRD is highly variable, which may suggest an intense variation of bedrock composition. However, investigation of HyLogging™ data from the seven diamond drill cores suggests that the variations of rock types are rather limited in the study area. The XRD analyses provide a very detailed picture of the mineral assemblage at single points, but clear patterns are difficult to establish for any rock type. In contrast, the HyLogging™ data measure many samples and allow a classification of rock types based on the major mineral assemblages and even the recognition of potential cross-cutting alteration. In addition, gradients in terms of changes in the abundance and composition of single mineral groups can be identified, which can help to identify vectors towards, for example, heavily altered and potentially mineralised horizons. However, our studies suggest that the extent of such alteration patterns recognisable with reflectance spectroscopy is only limited in the investigated rocks (i.e. less than ca. 5 m), which makes them virtually impossible to be detected using the ASTER Geoscience Products.

6.1.3. Saprolite

From the geochemical data, Salama et al. (2016–in this issue) postulated the division of the apparent saprolite into a lower ferruginous and upper kaolinitic saprolite. Elevated iron contents in geochemical analyses of the lower ferruginous saprolite may be related to weathering of ferro-magnesian minerals in bedrock. However, no ferro-magnesian minerals were detected in the saprolite samples using XRD. The absence of the ferro-magnesian minerals from the XRD data of the saprolite could be due to the instability of these minerals during weathering and/or limited thickness of the ferruginous saprolite, which is about 2.5 m according to the HyLogging™ data of NLD210 (Fig. 6).

XRD and FTIR analyses as well as HyLogging™ data all show that the upper kaolinitic saprolite is mainly composed of kaolinite and quartz. Based on the reflectance spectroscopic data, the kaolinite is predominantly well crystalline, which was used by previous studies to map in situ regolith (e.g. Cudahy et al., 2005). Towards the top of the saprolite, towards the silcrete in the hanging wall, the kaolinites are increasingly poorly crystalline. The change of the kaolin crystallinity below the silcrete layer can be attributed to leaching of residual kaolinite and reprecipitation of amorphous or poorly crystalline aluminosilicates and silica cement in the silcrete (Salama et al., 2016–in this issue). The continuous mineralogical gradients spanning the saprock and saprolite observed in the HyLogging™ data (e.g. gradual decrease of white mica and increase of kaolinite) suggest a weathering profile that developed in situ and was terminated by the silcrete.

6.1.4. Silcrete

Based on geochemical and petrographic analyses, Salama et al. (2016–in this issue) described siliceous units in the Neale tenement as silcrete that protects the in situ regolith profile from later erosion. XRD analyses of silcrete samples from the RC drill holes identify quartz as major component, but also minor amounts of kaolinite (Table 2). This complicates the differentiation of the silcrete from the transported material in the hanging wall, where many XRD results show the same mineral assemblage. In addition, kaolinites are poorly crystalline according to the hyperspectral data (Table 4), which could be used to interpret these intervals as originally transported material (sensu Cudahy, 1997). HyLogging™ data of drill core NLD210 show distinct layers in the silcrete that contain elevated amounts of kaolinite and iron oxides, whereas for major parts of the silcrete only quartz was detected (Fig. 6). The correct identification of this silcrete layer is significant for exploration in this area, as the silcrete prevents the vertical dispersion of geochemical alteration signatures, limiting the applicability of this exploration technique (González-Álvarez et al., in this issue-a,b).

6.1.5. Transported cover

The uppermost regolith horizon is only recorded in the RC drill hole data. According to the XRD results, the uppermost part of the transported cover horizon consists mainly of quartz, minor amounts of kaolinite and occasional primary minerals. The occurrence of unweathered primary minerals could be explained by their preservation in rock clasts derived by past and recent colluvial and alluvial processes that are or were sourced from other nearby areas. Reflectance spectroscopic data (HyLogging™ and FTIR) indicate well crystalline kaolinite at the base of this horizon changing to poorly crystalline kaolinite at the top (Figs. 3, 5). The change in kaolin crystallinity could point to leaching of clays and iron oxides at the top of the transported cover during humid periods and precipitation of these compounds as authigenic kaolinite and goethite at the base of the transported cover (Salama et al., 2016–in this issue).

6.2. Surface data

The ASTER Geoscience Products were used to interpret the mineralogy of erosional, depositional and relict environments comparable to the ones described from the Yilgarn Craton (Anand and Paine, 2002) and were further subdivided into regolith domains typical for the area studied (Table 4). According to the remote sensing data, the study area can be subdivided into four major sectors (Fig. 8):

1. dune fields (depositional) intersected by saprolite occurrences north of Neale and Hercules,
2. a levelled plateau (relict) surrounded to the east, south and west by erosional environments, including saprolite and Proterozoic bedrock-dominated terrains in the southwest (around Purple Haze and Voodoo Child),
3. highly separated sediment-dominated terrains in the southeast (depositional) with transported material sourced from the Proterozoic basement to the west, and
4. uniform sediment-dominated terrains in the east (depositional) with transported material sourced from the northern dune fields and underlying saprolite.

The northeast trending morphological boundary, visible in the DEM and almost all ASTER Geoscience Products, is a major feature that separates different regolith domains. However, almost orthogonal to this boundary, the regolith landforms are also split in further domains, probably governed to a high degree by the source of the transported material. For example, transported materials in the Hercules area were probably mainly sourced from the dune fields to the northwest, whereas the transported cover is rich in lateritic materials in the Atlantis area and probably sourced from the levelled plateaus and saprolite and bedrock-dominated terrains to the North of Purple Haze (Fig. 8). A schematic block model of the regolith landforms in the Hercules area is displayed in Fig. 9, which summarises the regolith landforms based on interpretations from the reflectance data. The southwestern part is dominated by saprolite and bedrock terrains (P) in an erosional breakaway environment (E), topped by a levelled plateau (GS) to the west. This levelled plateau changes to dune fields (Du) to the north of the Neale site (N). The flat plains of the dune fields are separated from lower flat plains (SD) by a northeast trending morphological boundary that consists possibly of silcretes (M). To the south, hardpans (H), for example around Atlantis (A), are developed in the lower flat plains, cross cut by drainage systems derived from the Proterozoic erosional area in the west.

6.3. Regolith characterisation and significance for exploration

Regolith settings of the Albany–Fraser Orogen were subdivided by González-Álvarez et al. (in this issue-a) into four domains: 1) Albany setting (shallow weathered profiles with minimal regolith thickness (i.e. 0 to 15 m), 2) Kalgoorlie–Norseman setting (intensely and variably deep weathering profile of at least 20 m and relict landscapes with erosional breaks), 3) Esperance setting (sand dunes with thin exposure of surface regolith stratigraphy), and 4) Neale setting. The latter one was described by Salama et al. (2016–in this issue) as a deeply weathered saprolitic profile in the Neale tenements of the northeastern Albany–Fraser Orogen, where a residual regolith profile, comprising saprock, lower ferruginous and upper kaolinitic saprolite and finally silcrete, is overlain by a transported blanket. The Neale setting was confirmed by the hyperspectral subsurface data. However, whereas the comparison of the subsurface and surface data in the case study area allowed the extrapolation of mineralogical and geochemical information acquired from the ground control points to a larger scale, the remote sensing data pointed to a variety of adjacent regolith environments. The study area features saprolite and bedrock dominated terrains, especially where Proterozoic granitoids and gneisses occur close to the current land surface. Furthermore, two types of sediment dominated terrains were developed in the area, namely 1) dune fields to the northwest and 2) alluvial/colluvial plains to the east, with the latter ones showing characteristic hematite-rich hardpans (sensu Anand and Paine, 2002) in the south of the study area, where erosional material derived from the Proterozoic bedrock is deposited. Drainage systems in this area discharge only over a short distance. The dune fields resemble the description of the northeastern part of the Albany–Fraser Orogen by Tille (2006), where sandplains, dunes and minor gravelly and calcrete plains dominate the Earth's surface.

The Neale and Hercules sites are located where silcretes are abundant in the regolith profile. In the whole northern area of Fig. 8 a deep in situ weathering profile (saprolite topped by mottled zone) can be expected below silcretes. To the south (towards Purple Haze and Voodoo Child) the Proterozoic bedrock is closer to the current surface and silcrete is not expected, resembling a Kalgoorlie–Norseman setting. The Atlantis site is located at the transition of these two domains, though being on the lower plains to the east of a northeast trending morphological step, the regolith is probably thinner than at Neale, for example, when assuming a rather levelled Mesozoic land surface. The thickness of transported regolith at Atlantis ranges between 10 and 15 m, whereas the in situ regolith is about 55 m (Salama et al., 2016–in this issue). The regolith material at Atlantis was not preserved during drilling and an estimation of the thickness of the saprolite versus transported material is difficult. But a distinct increase in iron oxide abundance might be related to the formation of lateritic materials at the surface, which were mapped using the ASTER data (Fig. 7).

The resulting regolith landform map (Fig. 8) shows significant differences to the published surface geological map (Stewart et al., 2008) and provides a much more detailed picture of regolith landforms in the Hercules area. The results of our regolith mapping study were summarised in a block model (Fig. 9) and the regolith landforms are

summarised in Table 4. The developed regolith map can be used to design transects through different regolith landforms.

The main mineralogical factors for detailed regolith characterisation comprise the abundance and type of Al-clays and iron oxides. Hyperspectral technologies are ideal to determine those critical factors. The classical example is the crystallinity of kaolinite, where transported sediments are typically characterised by poorly crystalline kaolinite whereas residual materials are dominated by well crystalline kaolinite (Cudahy, 1997). The ability to map out transported vs in situ regolith using hyperspectral remote sensing data was demonstrated by Cudahy et al. (2005), who released a kaolin crystallinity map of the Kalgoorlie map sheet. Such maps could be routinely generated for other areas using the respectively developed workflows. However, multispectral ASTER data do not have a sufficient spectral resolution to generate a kaolin crystallinity map, but still provide the option to distinguish Al-clay species (e.g. white mica vs. kaolinite) on a regional scale, as shown in our study (Table 4, Fig. 7).

The regolith interpretation from ASTER mineral maps can be compromised by vegetation (both green and dry) and fire scars. Green and dry vegetation have overlapping absorption features with major mineral groups and areas with more than ca. 60% green vegetation were masked out in the ASTER Geoscience Products used. Rodger and Cudahy (2009) and Haest et al. (2013) showed the potential for unmixing green vegetation from hyperspectral remote sensing data and a similar approach could also be applied to multispectral ASTER data. Fire scars were frequently observed in ASTER imagery in the northeastern Albany–Fraser Orogen and affected selected mineral maps, such as the AlOH Group Composition, where a fire scar is displayed to the northeast of NLD210 (Fig. 7a and b).

Mapping of erosional regimes using the ASTER Geoscience Products, validated by the subsurface data, is of major significance for gold exploration in the northeastern Albany–Fraser Orogen, and may be used to compare the Voodoo Child domain (sensu Doyle et al., 2015) with the Hercules domain. In addition, the identification of the source of transported material may help to find the reason for displaced geochemical anomalies in the Neale tenement (Salama et al., 2016–in this issue). For example, geochemical anomalies in the Atlantis area could be due to the accumulation of material that was sourced from the area around Purple Haze, as suggested by the ASTER Geoscience Products (Fig. 7) and the derived regolith landform products (Figs. 8, 9).

The main challenge to be tackled using these data is characterisation of the regolith cover for a test site in the Albany–Fraser Orogen of Western Australia, which has attracted recent exploration interest following the discoveries of the Tropicana Au and Nova Ni deposits (Doyle et al., 2015, Spaggiari and Pawley, 2012; Spaggiari et al., 2014a, b).

7. Conclusions

Multispectral remote sensing data in the form of ASTER Geoscience Products (Cudahy, 2011) and hyperspectral drill core logging data acquired with the HyLogging™ system were evaluated for mineral mapping in the Albany–Fraser Orogen of Western Australia, using XRD, FTIR and compared with results provided by Salama et al. (2016–in this issue). The evaluation was focussed on two main points, namely 1) mapping transported versus relict and erosional areas, and 2) characterisation of mineral assemblages that reflect the type of concealed bedrock and/or alteration systems possibly related to gold mineralisation.

The separation of transported from relict and erosional domains was achieved by using multispectral remote sensing (ASTER) and hyperspectral drill core logging (HyLogging™) data. Key mineral products, tracking the abundance and compositional variations of iron oxides and Al-clays, enable us to not only distinguish transported from erosional regimes, but also to relate depositional material to its source rocks and to identify the type of bedrock by characterising the mineralogy of its equivalent saprock.

This study shows that time consuming field-mapping could effectively be complemented by using mineral maps derived from multispectral remote sensing data in combination with a few ground control points (i.e. HyLogging™ data). Mineralogical characterisation of the regolith can be used to identify the respective depositional/erosional environment and provide insights to the concealed stratigraphy. This would help to target field work, to efficiently design drilling programmes, based on the information about the inferred composition and thickness of the overburden, and support the logging onsite by geologists.

Acknowledgements

The authors would like to thank MRIWA and GSWA for their support through the EIS programme, and especially to Beadell Resources Ltd., AngloGold Ashanti Australia, Creasy Group, Goldfields International Ltd., Sipa Resources Ltd. and Silver Lake (Integra Mining Ltd.) for their funding contribution. Tania Ibrahimi is thanked for her advice regarding geoinformatics. Mick Elias, Tom Cudahy, Ian Lau and an anonymous reviewer are thanked for their reviews of the manuscript and guest editor Mari Boni is acknowledged for handling the review process.

References

Anand, R.R., 2015. Weathering history, landscape evolution and implications for exploration: Australian perspective. Ore Geol. Rev. Spec. Issue (in this issue).
Anand, R.R., Paine, M., 2002. Regolith geology of the Western Australia: implications for exploration. Aust. J. Earth Sci. 49, 4–162.
Butt, C.R.M., 2016. The development of regolith exploration geochemistry in the Tropics and sub-tropics. Ore Geol. Rev. Spec. Issue 73, 380–393 (in this issue).
Caccetta, M., Collings, S., Cudahy, T.J., 2013. A calibration methodology for continental scale mapping using ASTER imagery. Remote Sens. Environ. 139, 306–317.
Cornell, R.M., Schwertmann, U., 2003. The iron oxides: structure, properties, reactions, occurrences and uses. 2nd edition.
Crowley, J.K., Vergo, N., 1988. Near-infrared reflectance spectra of mixtures of kaolin-group minerals: use in clay mineral studies. Clay Clay Miner. 36 (4), 310–316.
Cudahy, T.J., 1997. PIMA-II spectral characteristics of natural kaolins. CSIRO Exploration and Mining Report 420R (72 pp.).
Cudahy, T., 2011. Satellite ASTER Geoscience Product Notes Western Australia. http://c3dmm.csiro.au/WA_ASTER/stage_1_geoscienceproductnotes.html (23 pp.).
Cudahy, T., 2012. Satellite ASTER Geoscience Product Notes Australia. http://c3dmm.csiro.au/Australia_ASTER/stage_1_geoscienceproductnotes.html (23 pp.).
Cudahy, T.J., Caccetta, M., Cornelius, A., Hewson, R.D., Wells, M., Skwarnecki, M., Halley, S., Hausknecht, P., Mason, P., Quigley, M.A., 2005. Regolith geology and alteration mineral maps from new generation airborne and satellite remote sensing technologies and explanatory notes for the Kalgoorlie-Kanowna 1:100,000 scale map sheet, remote sensing mineral maps. MERIWA Report No. 252, 114 pp.
Cudahy, T., Hewson, R., Caccetta, M., Roache, A., Whitbourn, L., Connor, D., Mason, P., Yang, K., Huntington, J., Quigley, M., 2009. Drill core logging of plagioclase feldspar composition and other minerals associated with Archaean gold mineralization at Kambalda, Western Australia, using a bidirectional thermal infrared reflectance system. Rev. Econ. Geol. 16, 223–235.
Cudahy, T., Jones, M., Thomas, M., Laukamp, C., Caccetta, M., Hewson, R., Rodger, A., Verrall, M., 2008. Next Generation Mineral Mapping: Queensland airborne HyMap and satellite ASTER surveys 2006–2008. CSIRO report P2007/364 (161 pp.).
Doyle, M.G., Fletcher, I.R., Foster, J., Large, R.R., Mathur, R., McNaughton, N.J., Meffre, S., Muhling, J.R., Phillips, D., Rasmussen, B., 2015. Geochronological constraints on the Tropicana Gold Deposit and Albany–Fraser Orogen, Western Australia. Econ. Geol. 110, 355–386.
Ducart, D.F., Crosta, A.P., Souza, C.R., Coniclio, J., 2006. Alteration mineralogy at the Cerro La Mina epithermal prospect, Patagonia, Argentina: field mapping, shortwave infrared spectroscopy, and ASTER images. Econ. Geol. 101, 981–996.
Duuring, P., Hagemann, S., Novikova, Y., Cudahy, T., Laukamp, C., 2012. Targeting iron ore in banded iron formation using ASTER data: Weld Range greenstone belt, Yilgarn Craton, Western Australia. Econ. Geol. 107, 585–597.
Gallant, J.C., Dowling, T.I., Read, A.M., Wilson, N., Tickle, P., Inskeep, C., 2011. 1 second SRTM Derived Digital Elevation Models User Guide. Geoscience Australia (www.ga.gov.au/topographic-mapping/digital-elevation-data.html).
González-Álvarez, I., Anand, R.R., Boni, M., 2015b. Mineral Exploration in regolith-dominated terrains. Global considerations and challenges on a cratonic boundary: southeast Western Australia. Ore Geol. Rev. Spec. Issue (in this issue).
González-Álvarez, I., Salama, W., Anand, R.R., 2015a. Regolith framework of the Albany–Fraser Orogen, Western Australia. Ore Geol. Rev. Spec. Issue (in this issue).
Haest, M., Cudahy, T., Laukamp, C., Gregrory, S., 2012a. Quantitative mineralogy from visible to shortwave infrared spectroscopic data — I. Validation of mineral abundance and composition products of the Rocklea Dome channel iron deposit in Western Australia. Econ. Geol. 107, 209–228.
Haest, M., Cudahy, T., Laukamp, C., Gregrory, S., 2012b. Quantitative mineralogy from visible to shortwave infrared spectroscopic data — II. 3D mineralogical characterisation of the Rocklea Dome channel iron deposit, Western Australia. Econ. Geol. 107, 229–249.

Haest, M., Cudahy, C., Rodger, A., Laukamp, C., Martens, C., Caccetta, M., 2013. Unmixing vegetation from airborne visible-near to shortwave infrared spectroscopy-based mineral maps over the Rocklea Dome (Western Australia), with a focus on iron rich palaeochannels. Remote Sens. Environ. 129, 17–31.

Hewson, R.D., Cudahy, T.J., 2010. Geological mapping accuracy issues using ASTER in Australia. In: Ramachandran, B., Justice, C., Abrams, M. (Eds.), Applications in ASTER, Land Remote Sensing and Global Environmental Change: NASA's Earth Observing System and the Science of ASTER and MODIS. Springer, New York.

Hewson, R.D., Cudahy, T.J., Mizuhiko, S., Ueda, K., Mauger, A.J., 2005. Seamless geological map generation using ASTER in the Broken Hill-Curnamona province of Australia. Remote Sens. Environ. 99, 159–172.

Huntington, J.F., Mauger, A.J., Skirrow, R.G., Bastrakov, E.N., Connor, P., Mason, P., Keeling, J.L., Coward, D.A., Berman, M., Phillips, R., Whitbourn, L.B., Heithersay, P.S., 2005. Automated mineralogical logging of core from the emmie bluff, iron oxide copper–gold prospect, South Australia. Presented at the PACRIM 2004, Aus IMM publication series, Adelaide South Australia, pp. 223–230.

Kirkland, C.L., Spaggiari, C.V., Pawley, M.J., Wingate, M.T.D., Smithies, R.H., Howard, H.M., Tyler, I.M., Belousova, E.A., Poujol, M., 2011. On the edge: U–Pb, Lu–Hf, and Sm–Nd data suggests reworking of the Yilgarn craton margin during formation of the Albany–Fraser Orogen. Precambrian Res. 187, 223–247.

Laukamp, C., 2011. Short Wave Infrared Functional Groups of Rock-forming Minerals. CSIRO report EP115222.

Laukamp, C., 2013. Regolith landform mapping at the Oldfield well (Laverton Region, Western Australia) using ASTER. IGARSS 2013, 21.-26. July, Melbourne, Australia. IEEE Explore Volume (4 pp.).

Laukamp, C., Cudahy, C., Caccetta, M., Thomas, M., Close, D., Lennartz, R., 2013a. Successful mineral exploration using multispectral remote sensing data — ASTER Geoscience Map of Australia. SGA 2013, 12.-15. August, Uppsala, Finland (4 pp.).

Laukamp, C., Ramanaidou, E., Wells, M., Yang, K., 2013b. Kaolin and smectite group minerals in exploration and discovery. In: Gräfe, M., Klauber, C., McFarlane, A.A. (Eds.), Clays in the mineral resources value chain: a literature survey.— MERIWA report no. 300, Chapter 6, pp. 293–341.

Laukamp, C., Cudahy, T., Caccetta, M., Chia, J., Gessner, K., Haest, M., Liu, Y.C., Rodger, A., 2010. The uses, abuses and opportunities for hyperspectral technologies and derived geoscience information. AIG Bulletin, 51(Geo-Computing 2010 Conference, Brisbane, September 2010), pp. 73–76.

Laukamp, C., Termin, K.A., Pejcic, B., Haest, M., Cudahy, T., 2012. Vibrational spectroscopy of calcic amphiboles — applications for exploration and mining. Eur. J. Mineral. 24, 863–878.

Ninomiya, Y., Fu, B., Cudahy, T.J., 2005. Detecting lithology with Advanced Spaceborne Thermal Emission and Reflection Radiometer (ASTER) multispectral thermal infrared "radiance-at-sensor" data. Remote Sens. Environ. 99, 127–139.

Rodger, A., Cudahy, T., 2009. Vegetation corrected continuum depths at 2.20 μm: An approach for hyperspectral sensors. Remote Sens. Environ. 113, 2243–2257.

Rodger, A., Laukamp, C., Haest, M., Cudahy, T., 2012. A simple quadratic method of wavelength tracking for absorption features in continuum removed spectra. Remote Sens. Environ. 118, 273–283.

Rowan, L.C., Hook, S.J., Abrams, M.J., Mars, J.C., 2003. Mapping hydrothermally altered rocks at uprite, Nevada, using the Advanced Spaceborne Thermal Emission and Reflection Radiometer (ASTER), a new satellite-imaging system. Econ. Geol. 98, 1019–1027.

Salama, W., González-Álvarez, I., Anand, R.R., 2016. Significance of weathering and regolith/landscape evolution for mineral exploration in the NE Albany–Fraser Orogen, Western Australia. Ore Geol. Rev. Spec. Issue 73, 500–521 (in this issue).

Salisbury, J.W., Wald, A.E., 1992. The role of volume scattering in reducing spectral contrast of reststrahlen bands in spectra of powdered minerals. Icarus 96, 121–128.

Sonntag, I., Laukamp, C., Hagemann, S., 2012. Low potassium hydrothermal alteration in low sulfidation epithermal systems as detected by IRS and XRD: an example from the Co-O Mine, Eastern Mindanao, Philippines. Ore Geol. Rev. 45, 47–60.

Spaggiari, C.V., Pawley, M.J., 2012. Interpreted pre-Mesozoic bedrock geology of the Tropicana region of the east Albany–Fraser Orogen (1:250 000). In: The geology of the east Albany–Fraser Orogen — a field guide compiled by C.V. Spaggiari, C.L. Kirkland, M.J. Pawley, R.H. Smithies, M.T.D. Wingate, M.G. Doyle, T.G. Blenkinsop, C. Clark, C.W. Oorschot, L.J. Fox, and J. Savage, Geological Survey of Western Australia, Record 2011/23.

Spaggiari, C.V., Kirkland, C.L., Smithies, R.H., Occhipinti, S.A., Wingate, M.T.D., 2014b. Geological framework of the Albany–Fraser Orogen: extended abstracts. Geological Survey of Western Australia, Record 2014/6. pp. 12–27.

Spaggiari, C.V., Occhipinti, S.A., Korsch, R.J., Doublier, M.P., Clark, D.J., Dentith, M.C., Gessner, K., Doyle, M.G., Tyler, I.M., Kennett, B.L.N., Costelloe, R.D., Fomin, T., Holzschuh, J., 2014a. Interpretation of Albany–Fraser seismic lines 12GA–AF1, 12GA–AF2 and 12GA–AF3: implications for crustal architecture. In: Spaggiari, C.V., Tyler, I.M. (Eds.), Albany–Fraser Orogen Seismic and Magnetotelluric (MT) Workshop 2014: Extended Abstracts.- GSWA Record 2014/6.

Spaggiari, C.V., Kirkland, C.L., Pawley, M.J., Smithies, R.H., Wingate, M.T.D., Doyle, M.G., Blenkinsop, T.G., Clark, C., Oorschot, C.W., Fox, L.J., Savage, J., 2011. The Geology of the East Albany–Fraser Orogen — A field guide.—GSWA Record 2011/23.

Stewart, A.J., Sweet, I.P., Needham, R.S., Raymond, O.L., Whitaker, A.J., Liu, S.F., Phillips, D., Retter, A.J., Connolly, D.P., Stewart, G., 2008. Surface Geology of Australia 1:1,000,000 Scale, Western Australia [Digital Dataset].

Tappert, M., Rivard, B., Giles, D., Tappert, R., Mauger, A., 2013. The mineral chemistry, near-infrared, and mid-infrared reflectance spectroscopy of phengite from the Olympic Dam IOCG deposit, South Australia. Ore Geol. Rev. 53, 26–38.

Tille, P., 2006. Soil-landscapes of Western Australia's Rangelands and Arid Interior. Resource Management Technical Report 313 of the Department of Agriculture and Food, Government of Western Australia (153 pp.).

Witt, W.K., Hagemann, S.G., Ojala, J., Laukamp, C., Vennemann, T., Nykanen, V., 2013. Multiple methods for regional- to mine-scale targeting, Pataz gold field, northern Peru. Aust. J. Earth Sci. 61 (1), 43–58.

Yamaguchi, Y., Fujisada, H., Kudoh, M., Kawakami, T., Tsu, H., Kahle, A.B., Pniel, M., 1999. ASTER instrument characterization and operation scenario. Adv. Space Res. 23, 1415–1424.